Nano Energy 119 (2024) 109062

Contents lists available at ScienceDirect

Nano Energy

journal homepage: www.elsevier.com/locate/nanoen

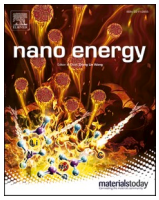

Vibration-coupled TENGs from weak to ultra-strong induced by vortex for harvesting low-grade airflow energy☆

Gao Yu [a,b,1], Jing Wen [b,c,1], Hao Li [b,c], Yurui Shang [a,b], Zhong Lin Wang [b,c,d,*,2], Baodong Chen [b,c,*,3]

[a] Center on Nanoenergy Research, School of Physical Science and Technology, Guangxi University, Nanning 530004, PR China
[b] Beijing Institute of Nanoenergy and Nanosystems, Chinese Academy of Sciences, Beijing 101400, PR China
[c] School of Nanoscience and Engineering, University of Chinese Academy of Sciences, Beijing 100049, PR China
[d] Georgia Institute of Technology, Atlanta, GA 030332-0245, USA

ARTICLE INFO

Keywords:
TENGs
Airflow energy harvesting
Vortex-induced vibration
Self-powered system

ABSTRACT

Multi-direction, irregularity, low-grade, the dynamic characteristics of low-grade airflow energy are prominent that making it difficult to collect. Here, we propose a vibration-coupled triboelectric nanogenerator (VC-TENG) induced by vortex to achieve from weak to ultra-strong vibration, thus effectively converting low-grade airflow energy into vibrational mechanical energy, and then electric energy. The transferred charge and short-circuit current increases is 47 and 26.9 times due to designed vortex structure, and the resonant response time is 2 s at a speed of 4.1 m/s. A VC-TENG unit delivers a peak power of 4.5 mW under a load resistance of 500 MΩ. A grouping of applied demonstrations of self-powered system validates the practicality and durability of VC-TENG. This work offers a practical strategy for harvesting low-grade airflow energy, and is a promising distributed power technologies for self-powered monitoring and forecasting system in the wild.

1. Introduction

Airflow energy is a ubiquitous and sustainable source of carbon-free energy with wide distribution and immense potential for power generation [1]. Traditional airflow energy harvesting primarily relies on wind turbines or energy conversion devices. However, in outdoor environments, the majority of airflow falls into the category of low-grade winds, where the wind speed is insufficient to meet the startup requirements of turbines [2]. Additionally, these low-grade winds are multi-directional and irregular, making it difficult for traditional turbines to effectively capture this energy. Consequently, there is significant promise and potential in collecting low-grade airflow energy for powering small electronic devices, particularly in outdoor or desert settings [3–6]. Conventional electromagnetic wind turbines are primarily designed to supply power to large-scale electrical grids and are not suitable for small mobile electronic devices, distributed sensors, or sensing systems [7–9] order to tackle this challenge, there is a pressing need to develop an innovative generator capable of effectively harvesting low-grade airflow to power microelectronic devices and distributed sensors.

Triboelectric nanogenerators (TENGs) exhibits tremendous potential for airflow energy harvesting due to its merits of low cost, [10–13] facile manufacturability,[14–19] high adaptability, [9,20–23] and a wide range of material options [18,21,24–31]. The current wind-driven triboelectric nanogenerators (TENGs) primarily rely on rotational structures, which typically require wind speeds higher than 5 m/s to achieve high output performance. However, most of the available wind speeds in the environment are within the range of gentle breeze (0–1.5 m/s) to moderate wind (3.4–5.4 m/s) [32]. Additionally, to achieve efficient energy harvesting, these reported TENGs generally adopt complex structures and sophisticated processes, which are not

☆ Prof Zhong Lin Wang, an author on this paper, is the Editor-in-Chief of Nano Energy, but he had no involvement in the peer review process used to assess this work submitted to Nano Energy. This paper was assessed, and the corresponding peer review managed by Professor Chenguo Hu, also an Associate Editor in Nano Energy.

* Corresponding authors at: Beijing Institute of Nanoenergy and Nanosystems, Chinese Academy of Sciences, Beijing 101400, PR China.
E-mail addresses: zlwang@gatech.edu (Z.L. Wang), chenbaodong@binn.cas.cn (B. Chen).
[1] These authors contributed equally: G. Yu, and J. Wen.
[2] 0000-0002-5530-0380
[3] 0000-0002-4647-0089

https://doi.org/10.1016/j.nanoen.2023.109062
Received 14 September 2023; Received in revised form 17 October 2023; Accepted 1 November 2023
Available online 4 November 2023

conducive to large-scale production and widespread use [33–35]. Thus, it is of great significance to design innovative structures for micro airflow energy harvesting that are simple, have low starting wind speeds, are portable, and have high efficiency to promote the practical application of wind-driven TENGs. Vortex-induced vibration (VIV) is a common phenomenon in fluid mechanics where the instability of airflow generates vortices [36]. The alternating effect of vortices influences the pressure distribution around objects, resulting in vibration. It can lead to fatigue failure and a shortened lifespan of structures, but it also signifies the potential to capture significant mechanical energy. In recent years, there has been extensive interest in effectively converting this energy into electricity. Traditional generators primarily employ piezoelectric and magneto-electric conversion technologies, but piezoelectric generators are limited by high stiffness and low cycle life, making them unsuitable for low airflow speeds and long-term operation. Electromagnetic generators are costly and complex, rendering them unsuitable for low-cost and maintenance-free applications. The combination of VIV phenomena with TENG technology for capturing airflow energy offers advantages such as efficient energy conversion, adaptability to low airflow speeds, multi-directional response, and flexible regulation. It is a highly promising technology for airflow energy harvesting.

Here, a vibration-coupled triboelectric nanogenerator (VC-TENG) was developed to efficiently harvest low-grade airflow energy with multi-directional and irregular characteristics using an arc-shaped structural strategy. The generator consists of a base, support rod, wind-direction tailfin, arc-shaped wind board, cylinder, and multiple power generation units. The power generation device is composed of polyamide (PA) balls, two copper electrodes and two fluorinated ethylene propylene (FEP) films. As airflow flows around the cylinder, the VC-TENG can induce vortex-induced vibrations over a wide range of wind speeds. Its startup wind speed can be as low as 1 m/s, a single TENG unit can produce an open-circuit voltage of 160 V, a transferred charge of 48nC, and a short-circuit current of 1.2μA. At a wind speed of 4.1 m/s, the peak power of the VC-TENG can reach 4.5 mW. The output performance of the VC-TENG remains essentially unchanged after more than 11,200 cycles during a continuous operation of 6.9 h, demonstrating its practicality and durability. Furthermore, we demonstrated its self-powered alarm system and wireless sensor powering, showcasing the potential applications of the VC-TENG.

2. Results and discussions

2.1. Structure design and working mechanism of VC-TENG

The VC-TENG is designed to efficiently harvest low-grade airflow energy to power electronic devices in desert environments. Fig. 1a presents a schematic diagram of the distributed power network based on the VC-TENGs array. The VC-TENG is driven by airflow, enabling sustained movement of the PA ball on the FEP film within the TENG unit. Typically, the motion or acceleration of a vibration-driven TENG indirectly affects the internal structure, and complex motion condition may not provide sufficient driving force for complete contact-separation. so minimizing vibration response is an effective method. This study will demonstrate the merits of this approach. Another advantage is that the commercial PA balls are very cheap, costing only about 6% of commercial PTFE balls and are easy to produce. Additionally, the mass density of PA is 0.95 g/cm^3, which is lower than PTFE 2.2 g/cm^3. The small PA balls could obtain a higher contact efficiency than large objects and achieve greater volume power density. The enlarged view of the TENG unit is shown in Fig. 1b. The TENG unit is composed of a PCB circuit board substrate, a surface copper foil, and FEP films and PA balls, with the PA ball located in the gap between the two FEP triboelectric layers.

The working principle of the TENG unit is shown in Fig. 1c. Driven by the wind, the PA balls collide and contact with the FEP films. During the contact electrification process, The PA balls acquire positive surface charges, and the FEP films obtain negative surface charges. The surface charges can persist for a long time as they are trapped electrons within potential well. (Fig. 1c(i)) shows the already-charged surfaces of both PA balls and FEP films. As PA balls move from the left to the right, the positive charges gradually induce negative electrons on the right electrode. The electrons flow back to the right electrode due to the electrostatic potential and generate the current in the circuit, as shown in (Fig. 1c(ii)). The current may exist before the PA ball reaches the right electrode. (Fig. 1c(iii)) shows the gathered PA balls in the right electrode. When the PA balls move back from right to left, the electrons gradually flow to the left electrode. The process generates a current in (Fig. 1c(iv)) opposite to the one in (Fig. 1c(ii)). The reciprocating motion of the PA balls will induce free electrons to flow between the two electrodes to produce alternating current. To better understand the output performance of the VC-TENG, the potential distribution of the two electrodes in different states was simulated by using the finite element analysis (commercial software of COMSOL Multiphysics). (Fig. 1d(i)) clearly shows the potential difference between the two electrodes when the dielectric balls are located on the left electrode. When the dielectric ball slide to the middle of the two electrodes, the potential become zero, as shown in (Fig. 1d(ii)), which drive current to flowing in the external circuit. Then, when the dielectric ball slide to the right electrode, the potential difference between the two electrodes is clearly shown in the potential profile in (Fig. 1d(iii)). When the dielectric ball is again located in the middle of the two electrodes, as shown in (Fig. 1d(iv)), the potential returns to zero, driving current to flow in the external circuit again. When the TENG unit is running at a wind speed of 4.1 m/s, its open circuit voltage, transfer charge and short-circuit current can reach 160 V, 48nC, and 1.2μA. As can be seen from Fig. 1**e-g**. To achieve energy harvesting from all wind directions, an adaptive wind-facing structure was designed, as shown in **Video S1** (Supporting Information).

Supplementary material related to this article can be found online at doi:10.1016/j.nanoen.2023.109062.

2.2. Vibration model and theoretical analysis of VC-TENG

The vibration induced by vortex shedding (VIV) is caused by the alternating shedding of vortices from the surface of the cylinder. As shown in Fig. 2a, When the fluid flows past the cylinder, it does so in an irregular and asymmetric manner on both sides, forming a series of alternating vortices. These vortices exert periodic lateral flow forces on the cylinder, leading to its oscillation.

When a cylinder is subjected to flow, it induces vortex shedding vibrations. The vibration of the cylinder under the influence of the flow can be regarded as a spring-mass-damping system [37–40]. The equation of motion for the cylinder can be expressed as:

$$m\ddot{y} + c\dot{y} + ky = \frac{1}{2}\rho U^2 D C_L \tag{1}$$

Where m, c, k is the mass, damping, and stiffness of the cylinder, ρ is the fluid density,D is the cylinder diameter, and U is the incoming flow velocity. C_L represents the coefficient of lift for the linear variation experienced by the cylinder. The y, $\dot{y}$, and $\ddot{y}$ are the displacement, velocity, and acceleration of motion. Using structural dynamic relationships: $\frac{c}{m} = 4\pi\xi f_n$, $\frac{k}{m} = \left(2\pi f_n^2\right)$. And using the relationship between mass ratios $m^* = \frac{4m}{\rho\pi D^2}$ (1) can be rewritten as:

$$\ddot{y} + 4\pi\xi f_n\dot{y} + \left(2\pi f_n^2\right)y = \frac{2U^2 C_L}{\pi m^* D} \tag{2}$$

Where $\xi$is the damping ratio of the structure, f_n is the natural frequency of the structure, and m^* is the mass ratio. The following dimensionless equation is further defined as follows:

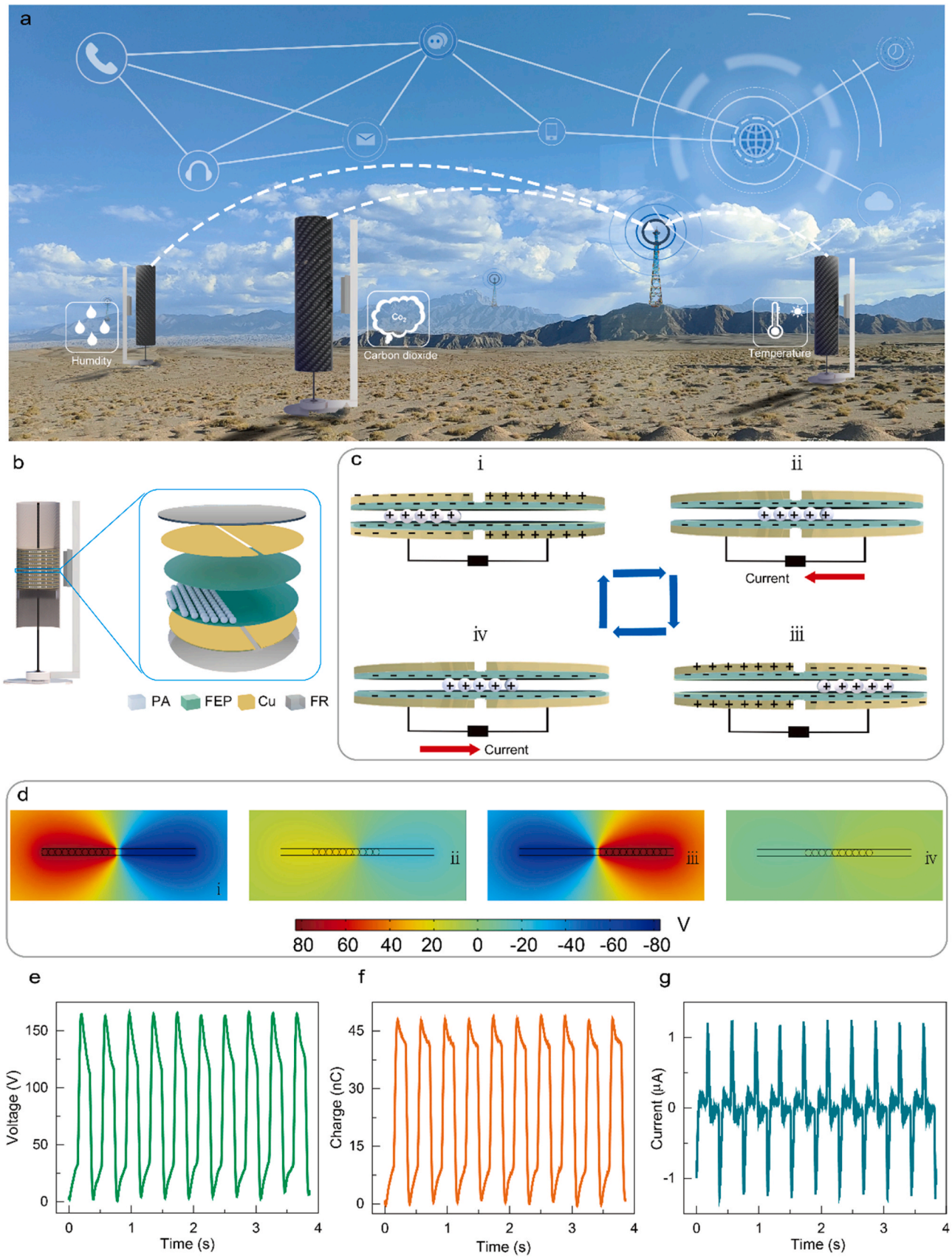

Fig. 1. Structure and working principle of VC-TENG. (a) Schematic of self-powered Gobi-desert monitoring system based on VC-TENG network for airflow energy harvesting. (b) Amplified structure and internal TENG units of VC-TENG. (c)Working principle and process of TENG units. (d) The corresponding potential distribution calculated by COMSOL in a 2D plane. (e) Open circuit voltage waveform. (f)Transfer charge quantity waveform. (g) Short-circuit current waveform.

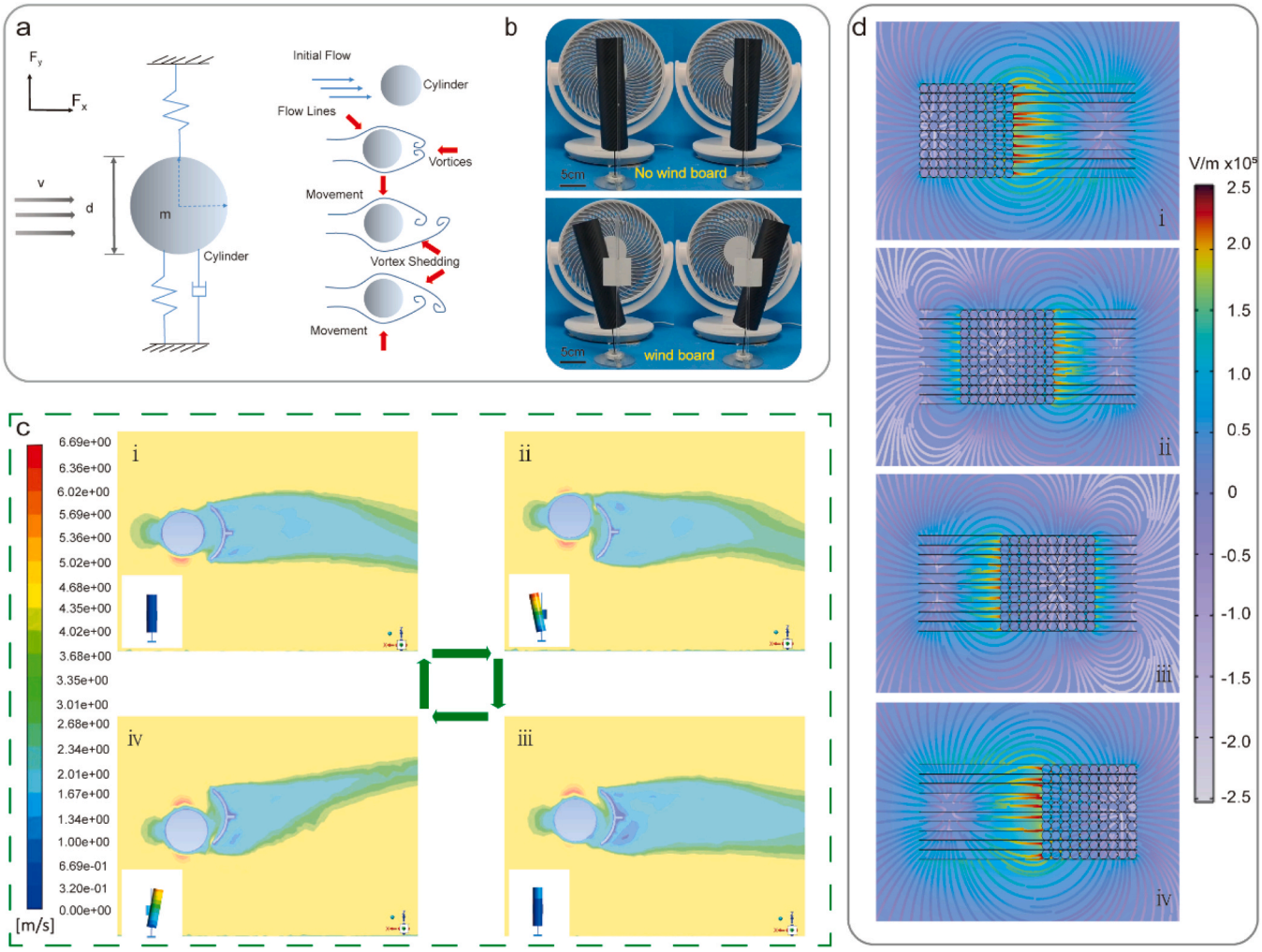

Fig. 2. Dynamic fluid-structure interaction analysis and electric field simulation of VC-TENG. (a) Dynamic fluid-structure interaction analysis of VC-TENG. (b) Vibration amplitude of VC-TENG with and without arc-shaped wind board. (c) Vibration simulation and surrounding vortex characteristics of VC-TENG (using ANSYS software). (d) The corresponding electric field distribution calculated by COMSOL in a 2D plane.

$$\ddot{Y} = \frac{\ddot{y}D}{U^2} \quad \dot{Y} = \frac{\dot{y}}{U} \quad Y = \frac{y}{D} \quad F_n = \frac{f_n D}{U} \tag{3}$$

Substituting Eq. (3) into Eq. (2) yields the dimensionless equation for structural vibration:

$$\ddot{Y} + 4\pi\xi F_n \dot{Y} + (2\pi F_n)^2 Y = \frac{2C_L}{\pi m^*} \tag{4}$$

The detailed derivation process is described in **note S1** (Supporting Information). In a Kármán vortex street, fluid forms a vortex structure as it flows around a bluff structure. The vortex itself is a concentration of energy that absorbs the fluid's kinetic and pressure energy and converts it into kinetic and pressure energy within the vortex. When the vortex reaches a certain strength, it generates a pressure field in the fluid, resulting in a Kármán vortex street. Therefore, the formation of vortices and the conversion of energy are the primary reasons for the occurrence of Kármán vortex street-induced vibration. [41] Fig. 2b shows the oscillation amplitude with and without the arc-shaped wind board. As shown in **video S2** (Supporting Information), It can be observed that the motion is more pronounced with the presence of the arc-shaped wind board compared to the absence of the arc-shaped wind board. There may be two possible reasons for this. Firstly, the arc-shaped wind board can reduce the scale of the vortex, making it easier to peel off. In this context, the scale of vortex refers to the size of the vortex region. When there is no arc-shaped wind board present, there is a vast space behind the cylinder. In this scenario, the vortex generated propagate backward along the flow direction, resulting in a larger-scale vortex formation. Correspondingly, the energy density within the entire vortex is lower, leading to a smaller vortex-induced force. Consequently, the vortex has difficulty detaching from the surface of the cylinder. However, when the arc-shaped wind board is introduced, the shape of the arc-shaped wind board facilitates the formation of vortex more effectively, and the wind board restricts the expansion space for the vortex, reducing its scale. In this situation, the energy density within the vortex increases, leading to a higher vortex-induced force. As a result, the vortex is more prone to detachment from the surface of the cylinder.

Supplementary material related to this article can be found online at doi:10.1016/j.nanoen.2023.109062.

Secondly, the arc-shaped wind board can also increase the frequency of the vortex. The vortex frequency is related to its scale and flow velocity. By appropriately designing the shape and positioning of the arc-shaped wind board, it is possible to modify the scale and velocity of the vortices, thereby increasing their frequency and enhancing vortex shedding. This leads to more intense forces acting on the cylinder, resulting in larger oscillations. The dynamic stress analysis of VC-TENG under mechanical and external airflow conditions was simulated using ANSYS software, as shown in **video S3** (Supporting Information). Then, the interaction between the cylinder, arc-shaped wind board, and airflow was simulated using FLUNT software, as shown in **video S4**

(Supporting Information). The motion state of VC-TENG and the formation of synchronous vortices are shown in Fig. 2c. In fluid dynamics, when airflow passes through a cylinder at a certain velocity, vortices are generated behind the cylinder, and the arc-shaped wind board can enhance the vortices. This may be one of the reasons why VC-TENG can collect airflow energy at low wind speeds. Fig. 2d shows the variation of the electric field strength of VC-TENG during the motion process, which was simulated using the finite element analysis method (Commercial software of COMSOL Multiphysics).

Supplementary material related to this article can be found online at doi:10.1016/j.nanoen.2023.109062.

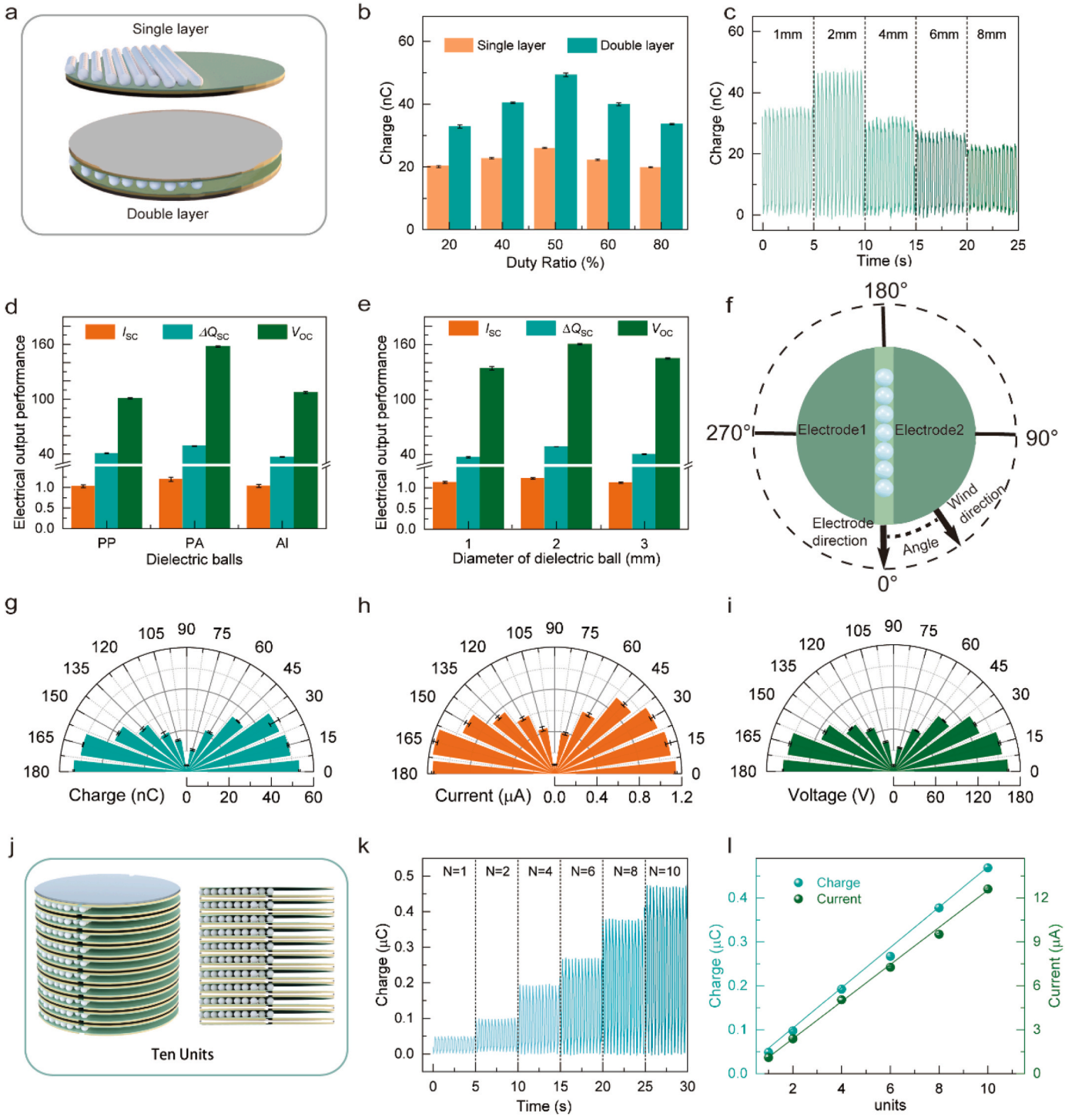

Fig. 3. Structure optimization of VC-TENG unit. (a) Single and double triboelectric layers of VC-TENG unit. (b) Transferred charge of single and double triboelectric layers with PA balls at different duty ratios. (c) Transferred charge at different electrode gaps. (d) Electrical output performance measured with balls of Different Materials. (e) Electrical output performance of different diameter PA balls (f) Definition of the angle between wind direction and electrode direction. (g) Transferred charge, (h) Short-circuit current and (i) Open-circuit voltage change from 0°−180°. (j) Schematic of multi-layer VC-TENG. (k) Transferred charge measured for different numbers of VC-TENG units. (l) The transferred charge and current exhibit nearly linear proportionality with the number of VC-TENG units.

2.3. Structural optimization of VC-TENG

The Number of PA balls and triboelectric layers, contact area, and electrode gap are the essential structural parameters of a TENG unit. Fig. 3a shows a schematic of the components of a TENG unit. The number of PA balls in the unit space is crucial to achieving the optimal output. The duty ratio, defined as the ratio of the volume occupied by the PA balls in the TENG unit, can describe the amount. Fig. 3b compares the electrical output performance between different duty ratios. In the experiment, an upper empty half-open TENG unit was first used to study the electrical output performance. It can be seen from Fig. 3b that the output performance is optimal when the duty ratio of the balls is 50%, with a corresponding transferred charge of 25 nC. The half-open TENG has only one layer of FEP films which limited the surface charge density. With double-layer FEP films and 50% duty ratio, the transfer charges reached 48 nC. The double triboelectric layers produce more surface charges than a single triboelectric layer. The corresponding open-circuit voltage and short-circuit current are detailed in Fig. S1(Supporting Information). However, the transfer charges begin to decrease when the duty ratio over 50%, possibly because as the number of PA balls increases and occupies more space, the balls cannot fully move from one electrode to another, while duty ratio lower than 50% will reduce the corresponding contact area. By measuring the unit weight and vibration conditions, 50% duty ratio would be the optimal parameter. The width of the gap between the left and right electrodes also affects the electrical output performance. The electrical output performance was investigated for gap widths of 1 mm, 2 mm, 4 mm, 6 mm, and 8 mm. From Fig. 3c, it can be observed that at a gap width of 2 mm, the maximum transfer charges are approximately 48nC. The open-circuit voltage and short-circuit current are shown in Fig. S2(Supporting Information). There may be two reasons for this. One is that the diameter of the PA balls is 2 mm, and a gap of 2 mm is sufficient to accommodate the independent process of the PA balls. Another reason may be the working area. During the idle period of motion, the PA balls had the tendency to accumulate at the corner, while a few PA balls remained behind. The gap of 1 mm makes the balls insufficient to generate an independent process, while gap widths of 4 mm, 6 mm, and 8 mm reduce the working area of the PA balls. In these cases, more PA balls are in the gap area, contributing little to the transfer charges. In addition, the material selection of the balls should be considered during optimization. Although there are a wide range of material choice and potential modification, PA balls are still a representative choice. As shown in Fig. 3d, it can be seen that the output performance of PA balls is optimal. Fig. 3e compares the output performance of PA balls with different diameters, and the output is optimal with a diameter of 2 mm. The lower output of 1 mm balls may be due to their smaller size and lighter weight, resulting in smaller accelerations., and the other reason is that 1 mm balls are more prone to electrostatic adsorption, which restricts their movement. The utilization rate of 3 mm balls is smaller than that of 2 mm balls, and their weight is larger. Generating less motion under the same driving force. The ability of the TENG to collect vibration energy from any direction was also studied. The direction is defined as the intersection angle between the electrodes direction and the vibration motion, as shown in Fig. 3f. Fig. 3g-i displays the measured transfer charges, short-circuit current, and open-circuit voltage for angles ranging from 0° to 180°. It can be seen from Fig. 3g that the transfer charges are highest at 0° and 180°, and lowest at 90°. This is mainly because at angles of 0° and 180°, the PA balls moved completely from one electrode to the other, while at 90°, the PA balls mainly moved on a single electrode, resulting in minimal charge transfer through the external circuit. The short-circuit current and open-circuit voltage also reflected the changes caused by the directions that can be seen from the Figure3h-i. Detailed results for the 0–180° direction can be found in Fig. S3 (Supporting Information). Therefore, the VC-TENG can harvest airflow energy from any direction and is more suitable for directions that can provide enough motion to separate the PA balls from one electrode to another. From the results, it can be concluded that the device's output performance is optimal at 0°and 180°, worst at 90°. Multiple TENG units were combined and placed inside a cylinder to increase the volume power density of the entire VC-TENG, as shown in Fig. 3j. When the wind drives the TENG, all units can simultaneously collect airflow energy and work effectively. Fig. 3k shows the relationship between the number of units and the transferred charge. It can be seen that the output performance increases linearly with the increase in the number of units, as shown in Fig. 3l. The corresponding short-circuit current can be found in Fig. S4 (Supporting Information).

The external structural parameters of VC-TENG are also key factors that affect its output performance. As shown in Fig. 4a, we first studied the electrical output performance under different curvatures of the arc-shaped wind board and wind speeds, the transfer charges can be observed to increase with the increment of curvature and wind speed in Fig. 4b until reaching a stable state, When the curvature is 25 and the wind speed is 4.1 m/s, the transfer charges can reach 0.47 μC. The corresponding current is shown in Fig. 4c, and when the curvature is 25 and the wind speed is 4.1 m/s, the current can reach 12.3 μA. Secondly, considering the influence of the distance between the arc-shaped wind board and the cylinder and the height of the position of the arc-shaped wind board on the swinging effect, as shown in Fig. 4d. the electrical output performance was studied under different distances between the arc-shaped wind board and the cylinder. The distance is defined as the distance from the center of the arc length of the arc-shaped wind board to the cylinder wall, When the distance is 2 cm, the highest transfer charges are 0.46 μC, and the short-circuit current is 12.2 μA. as shown in Fig. 4e. The swinging effect is not good when the arc-shaped wind board is 1 cm or 3 cm from the cylinder, it is possible that at a distance of 1 cm, there is not enough space between the arc-shaped wind board and the cylinder to generate vortices, and the corresponding eddy current force is very small or even non-existent. When the arc-shaped wind board is positioned 3 cm away from the cylinder, the flow field between the cylinder and the arc-shaped wind board will weaken, and the resulting eddy current force will be smaller, which will make the swing of the cylinder smaller. Therefore, the optimal distance between the arc-shaped wind board and the cylinder is 2 cm. The height of the arc-shaped wind board also affects the performance of the structure. As shown in Fig. 4f. The electrical output performance of the arc-shaped wind board at different heights was tested. The height is defined as the distance from the bottom of the arc-shaped wind board to the rotating support base. The maximum output value is achieved when the height of the arc-shaped wind board is 12.5 cm, with a corresponding transfer charges of approximately 0.47 μC and a short-circuit current of approximately 12.4 μA. It is possible that when the height is 12.5 cm, the center of the arc-shaped wind board coincides with the center of the cylinder, and at this point, the elastic support rod is in an optimal state with balanced force deformation and elastic recovery. When the arc-shaped wind board is lower, the elastic support rod is less prone to deformation, and a greater excitation force is required for it to vibrate. When the arc-shaped wind board is higher, its elastic support rod is more prone to deformation, but its recovery deformation cycle is longer, resulting in a lower swing frequency and a decrease in the overall structural output performance. The aspect ratio of the arc-shaped wind board also has a significant impact on the swing of the cylinder. The aspect ratio of the arc-shaped wind board as shown in Fig. 4g, affects the cylinder differently when the wind blows over it. as shown in Fig. 4h, the transfer charges increase with the increase in the size of the arc-shaped wind board until it tends to stabilize. Fig. 4i shows the change in the short-circuit current also increases first and then tends to stabilize. The size of the arc-shaped wind board has a significant influence on the formation and shedding of vortices. As can be seen from Fig. 4h-i, when the size is 50 × 50 mm, the transfer charges and short-circuit current tend to be stable, possibly because the 50 × 50 mm arc-shaped wind board is the same diameter size as the cylinder, and the fluid flowing through the cylinder can be compressed by the arc-shaped wind board within this range, making it less likely to diverge and easier to shed

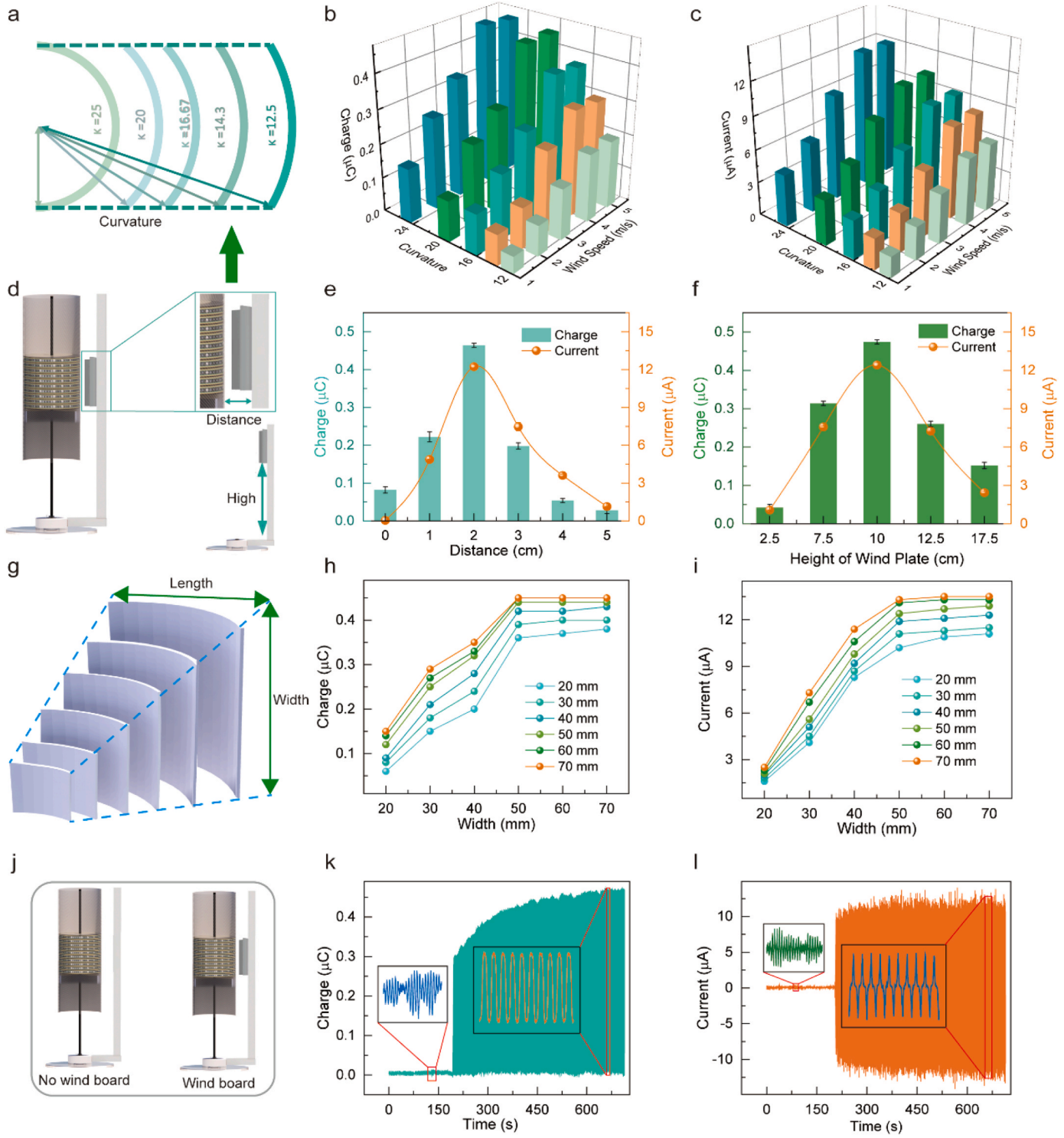

Fig. 4. Performance optimization of VC-TENG. (a) Different curvature parameters of wind board of VC-TENG. (b) Transferred charge and (c) Short-circuit current at different curvatures and wind speeds. (d) Distance between the arc-shaped wind board and the cylindrical body, and height of the arc-shaped wind board from the rotating support base. (e) Transferred charge and short-circuit current at different distances (f) Transferred charge and short-circuit current at different heights (g) Arc-shaped wind board with different length-to-width ratios. (h) Transferred charge and (i) Short-circuit current at different length-to-width ratios of arc-shaped wind board. (j) Comparison of device structure with and without arc-shaped wind board. (k) transferred charge and (l) short circuit current with and without arc-shaped wind board.

vortices. When the size continues to increase, the compressing effect on the vortices is not significant, and the corresponding electrical output performance is relatively stable with no significant changes.

The electrical output performance was tested with and without the arc-shaped wind board. Fig. 4j shows the schematic diagram of the device structure with and without the arc-shaped wind board. Without the arc-shaped wind board, the transfer charges were about 0.01 μC and the short-circuit current was 0.48 μA. With the arc-shaped wind board, the corresponding transfer charges increased to 0.47 μC and the short-circuit current increased to 12.9 μA, as shown in Fig. 4k-l. Compared

to the case without the arc-shaped wind board, the transfer charges increased by about 47 times and the short-circuit current increased by about 26.9 times. To better evaluate the output performance of the VC-TENG, according to calculations, the energy output per unit volume of VC-TENG can reach 2.3 W/m^3.

2.4. Performance and applications demonstration of VC-TENG

A self-powered environmental monitoring system based on airflow energy harvesting was developed for distributed desert monitoring applications, as shown in Fig. 5a. In this system, the VC-TENG collects and converts airflow energy in the environment into electrical energy, which is then managed and stored by the power management circuit to supply power to the load. The schematic diagram of the power management circuit is shown in Fig. 5b. In addition, Fig. 5c shows the charging performance of the VC-TENG using different capacitors. When operating at a wind speed of 4.1 m/s, the voltage of the capacitors from 10, 22, 47, 100,220and 4700 μF are reached 26.4, 16, 7.4, 3.1,2.2, and 1 V in the charging time of 200 s, in order to evaluate the impedance matching and peak power of the VC-TENG device, its output performance was tested with a series of different load resistances at a wind speed of 4.1 m/s, as illustrated in Fig. 5d. When the resistance is small, the output current showed a horizontal trend. Then the output current gradually decreased as the external load resistance increased, and the output power rise and then falls. A peak power of 4.5 mW was obtained at a load resistance of 500 MΩ. Additionally, after continuous testing for 6.9 h (over 11,200

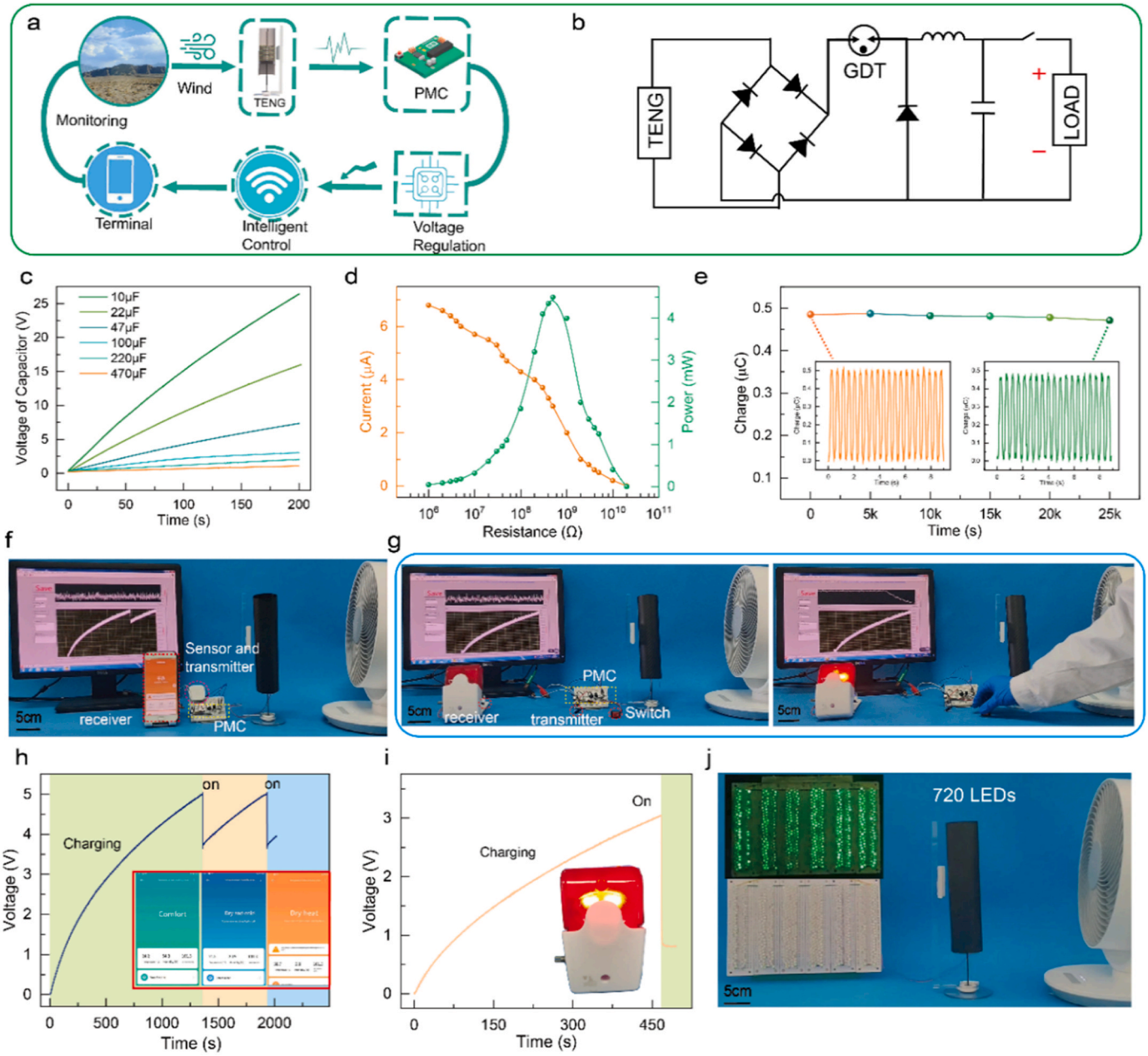

Fig. 5. Applications Demonstration of VC-TENG. (a) Schematic process of VC-TENG for self-powered environmental monitoring. (b) PMC Circuit Schematic. (c) Voltage profiles of the capacitor with different capacitance charged by the VC-TENG. (d) The output power and instantaneous peak current-resistance relationship profiles for the VC-TENG. (e) Durability test of VC-TENG at a wind speed of 4.1 m/s for over 6.9 h. (f) Photos and demonstrations of a self-powered weather monitoring system. (g) Photos and demonstrations of a self-powered emergency alarm system. (h) Voltage profile of self-powered weather monitoring system during charging and discharging. (i) The voltage profile of the self-powered emergency alarm system during the charging and discharging process. (j) 720 LEDs lighted up by the VC-TENG.

cycles), as shown in Fig. 5e and Fig. S5 (Supporting Information), the transfer charges of the VC-TENG still remained at 97.9%, Environmental monitoring technology can provide big data support for outdoor or Gobi-desert oil exploration, development, and production, and is of great significance for desertification prevention and climate change research. The output energy of the VC-TENG is first rectified and stored in a 680 μF capacitor through a bridge rectifier and a PMC. Next, the commercial energy harvesting power chip LTC3588 is used to further stabilizes the electrical energy and generate stable voltage to drive the temperature/humidity sensor and transmitter. The circuit connection diagram of the LTC3588 as shown in Fig. S6 (Supporting Information). In the experiment, the mobile phone and transmitter are connected through the Wi-Fi network, enabling remote transmission of meteorological signals as shown in Fig. 5f. The voltage versus time is shown in Fig. 5h. After initial charging a 680μF capacitor for 22 min, the power management circuit can generate 5 V voltage to drive the sensor and transmitter to work for the first time. Then the phone can receive temperature/air pressure/humidity signals from the system approximately every 9 min. The corresponding visual demonstration can be found in **Video S5** (Supporting Information). A self-powered emergency alarm system has been developed, consisting of a rectifier bridge, PMC, 680 μF capacitor, and signal transmitter unit. The Photograph of the self-powered emergency alarm system and receiving terminal are exhibited in Fig. 5g. The voltage curve of the self-powered emergency alarm system during charging and discharging is shown in Fig. 5i. When the charging time of the capacitor exceeds 467 s, the switch is closed and the transmitter is powered for sending a warning signal, then the remote signal receiver will be triggered and are given voice or the alarm signal light, as shown in **Video S6** (Supporting Information). In addition, the VC-TENG can drive 720 LED lights, as shown in Fig. 5j and **Video S7** (Supporting Information), which can provide lighting and direction guidance for pedestrians and passing vehicles at night. These applications demonstrate that VC-TENG can harvest airflow energy to meet energy supply requirements.

Supplementary material related to this article can be found online at doi:10.1016/j.nanoen.2023.109062.

3. Conclusion

In summary, we reported a new triboelectric nanogenerator (VC-TENG) utilizing vortex-induced vibration for harvesting low-grade airflow energy. Benefitting from the arc-shaped structure strategy, the vibration from weak to ultra-strong is realized, its presence enhances the transferred charge by 47 times, increases the short-circuit current by 26.9 times. At a wind speed of 4.1 m/s, the peak power can reach 4.5mw. Coupled with a power management circuit (PMC), the VC-TENG can be utilized as a distributed direct-current power source for driving electronics. A series of applications, including self-powered emergency alarm systems, self-powered signal light systems, and self-powered meteorological monitoring systems, have been developed and successfully verified for practicality and durability in airflow energy harvesting in the Gobi-desert. This work gives a new strategy to improve the harvesting efficiency of low-grade airflow energy, but also as a self-charging power cell exhibits large potential for building sustainable self-powered monitoring and forecasting system in the future.

4. Experimental section

4.1. Fabrication of VC-TENG

The components of VC-TENG mainly consist of a carbon fiber tube (diameter 50 mm, height 250 mm, wall thickness 0.5 mm) serving as the induced pole, a glass fiber rod (diameter 2 mm, height 250 mm) serving as the support pole, a base (made by UV-cured 3D printing), a ceramic bearing (605CE/P2), an arc-shaped wind board (made of resin), a tail fin (made of acrylic), a connecting structure (which allows the carbon fiber and glass fiber to be concentrically connected, made by UV-cured 3D printing), and an embedded power generation unit. The tail fin and ceramic bearing are connected to the outer ring of the base by designing corresponding slots to maintain a certain height with the base, and the carbon fiber tube and glass fiber are connected to the base through the connecting structure. The power generation unit is then placed inside the carbon fiber tube, and the arc-shaped wind board is placed at the center of height of the tail fin.

A single TENG unit primarily consists of PA balls (diameter 2 mm), PCB circuit board (diameter 50 mm, thickness 0.3 mm), FEP films (thickness 30 μm), and a ring clamp (UV-cured 3D printed). The PCB circuit board adopts a bare copper process, with one side of the substrate covered in copper while the other side is not. The side with copper features two semi-circular copper areas with a certain gap (electrode gap). The FEP films is adhered to the side of the PCB circuit board with copper, Two PCB circuit board substrates coated with FEP films are placed vertically with a 2 mm spacing, and the PA balls are positioned within the 2 mm gap. Subsequently, a ring clamp is utilized to secure the assembly. The entire VC-TENG consists of ten TENG units.

4.2. Characterization and measurement

The single TENG unit is driven by a linear motor (R-LP3). The open-circuit voltages, short-circuit currents and transferred charges of VC-TENG were measured by the low-noise voltage preamplifiers (Keithley 6514 system electrometer). A programmed LabVIEW interface was used to realize real time data acquisition. The airflow was simulated by an electric fan. A commercial anemometer was used to measure wind speed.

CRediT authorship contribution statement

Gao Yu: Writing – original draft preparation, Methodology. **Jing Wen**: Data curation, Validation. **Hao Li:** Visualization. **Yurui Shang:** Investigation. **Zhong Lin Wang:** Supervision, Resources, Writing – review & editing. **Baodong Chen:** Conceptualization, Writing – review & editing, Supervision, Resources. All authors contributed to the manuscript.

Declaration of Competing Interest

The authors declare that they have no known competing financial interests or personal relationships that could have appeared to influence the work reported in this paper.

Data availability

No data was used for the research described in the article.

Acknowledgments

G. Yu, and J. Wen contributed equally to this work. The authors acknowledge the support from the National Natural Science Foundation of China 52192610), and the National Key R & D Project from Minister of Science and Technology (2021YFA1201601).

Appendix A. Supporting information

Supplementary data associated with this article can be found in the online version at doi:10.1016/j.nanoen.2023.109062.

References

[1] B. Chen, Y. Yang, Z.L. Wang, Scavenging wind energy by triboelectric nanogenerators, Adv. Energy Mater. 8 (2018), 1702649, https://doi.org/10.1002/aenm.201702649.

[2] Q. Zeng, Y. Wu, Q. Tang, W. Liu, J. Wu, Y. Zhang, G. Yin, H. Yang, S. Yuan, D. Tan, C. Hu, X. Wang, A high-efficient breeze energy harvester utilizing a full-packaged triboelectric nanogenerator based on flow-induced vibration, Nano Energy 70 (2020), 104524, https://doi.org/10.1016/j.nanoen.2020.104524.
[3] Z. Ren, Z. Wang, Z. Liu, L. Wang, H. Guo, L. Li, S. Li, X. Chen, W. Tang, Z.L. Wang, Energy harvesting from breeze wind (0.7–6 m s $^{-1}$) using ultra-stretchable triboelectric nanogenerator, Adv. Energy Mater. 10 (2020), 2001770, https://doi.org/10.1002/aenm.202001770.
[4] S.S. Kwak, S.M. Kim, H. Ryu, J. Kim, U. Khan, H.-J. Yoon, Y.H. Jeong, S.-W. Kim, Butylated melamine formaldehyde as a durable and highly positive friction layer for stable, high output triboelectric nanogenerators, Energy Environ. Sci. 12 (2019) 3156–3163, https://doi.org/10.1039/c9ee01267b.
[5] H. Oh, S.S. Kwak, B. Kim, E. Han, G.H. Lim, S.W. Kim, B. Lim, Highly conductive ferroelectric cellulose composite papers for efficient triboelectric nanogenerators, Adv. Funct. Mater. 29 (2019), 1904066, https://doi.org/10.1002/adfm.201904066.
[6] G. Li, J. Wang, S. Fu, C. Shan, H. Wu, S. An, Y. Du, W. He, Z. Wang, W. Liu, Y. Nie, S. Liu, P. Wang, C. Hu, A nanogenerator enabled by a perfect combination and synergetic utilization of triboelectrification, charge excitation and electromagnetic induction to reach efficient energy conversion, Adv. Funct. Mater. 33 (2023), https://doi.org/10.1002/adfm.202213893.
[7] B.-G. Park, C. Lee, Y.-J. Kim, J. Park, H. Kim, Y. Jung, J.S. Ko, S.-W. Kim, J.-H. Lee, H. Cho, Toxic micro/nano particles removal in water via triboelectric nanogenerator, Nano Energy 100 (2022), 107433, https://doi.org/10.1016/j.nanoen.2022.107433.
[8] Y. Wang, T. Chen, S. Sun, X. Liu, Z. Hu, Z. Lian, L. Liu, Q. Shi, H. Wang, J. Mi, T. Zhou, C. Lee, M. Xu, A humidity resistant and high performance triboelectric nanogenerator enabled by vortex-induced vibration for scavenging wind energy, Nano Res. 15 (2021) 3246–3253, https://doi.org/10.1007/s12274-021-3968-9.
[9] H. Li, J. Wen, Z.Q. Ou, E.R. Su, F.J. Xing, Y.H. Yang, Y.S. Sun, Z.L. Wang, B. D. Chen, Leaf-Like TENGs for harvesting gentle wind energy at an air velocity as low as 0.2 m/s, Adv. Funct. Mater. 33 (2023), 2212207, https://doi.org/10.1002/adfm.202212207.
[10] X. Gao, F. Xing, F. Guo, Y. Yang, Y. Hao, J. Chen, B. Chen, Z.L. Wang, A turbine disk-type triboelectric nanogenerator for wind energy harvesting and self-powered wildfire pre-warning, Mater. Today Energy 22 (2021), 100867, https://doi.org/10.1016/j.mtener.2021.100867.
[11] S. Yuan, Q. Zeng, D. Tan, Y. Luo, X. Zhang, H. Guo, X. Wang, Z.L. Wang, Scavenging breeze wind energy (1–8.1 ms^{-1}) by minimalist triboelectric nanogenerator based on the wake galloping phenomenon, Nano Energy 100 (2022), 107465, https://doi.org/10.1016/j.nanoen.2022.107465.
[12] S. Cheon, H. Kang, H. Kim, Y. Son, J.Y. Lee, H.-J. Shin, S.-W. Kim, J.H. Cho, High-performance triboelectric nanogenerators based on electrospun polyvinylidene fluoride-silver nanowire composite nanofibers, Adv. Funct. Mater. 28 (2018), 1703778, https://doi.org/10.1002/adfm.201703778.
[13] C. Shan, W. He, H. Wu, S. Fu, Q. Tang, Z. Wang, Y. Du, J. Wang, H. Guo, C. Hu, A high-performance bidirectional direct current TENG by triboelectrification of two dielectrics and local corona discharge, Adv. Energy Mater. 12 (2022), https://doi.org/10.1002/aenm.202200963.
[14] D. Liu, B. Chen, J. An, C. Li, G. Liu, J. Shao, W. Tang, C. Zhang, Z.L. Wang, Wind-driven self-powered wireless environmental sensors for Internet of Things at long distance, Nano Energy 73 (2020), 104819, https://doi.org/10.1016/j.nanoen.2020.104819.
[15] S.S. Kwak, H.-J. Yoon, S.-W. Kim, Textile-based triboelectric nanogenerators for self-powered wearable electronics, Adv. Funct. Mater. 29 (2019), 1804533, https://doi.org/10.1002/adfm.201804533.
[16] Y. Yang, L. Zheng, J. Wen, F. Xing, H. Liu, Y. Shang, Z.L. Wang, B. Chen, A swing self-regulated triboelectric nanogenerator for high-entropy ocean breaking waves energy harvesting, Adv. Funct. Mater. (2023), 2304366.
[17] J. Zhang, Y. Sun, J. Yang, T. Jiang, W. Tang, B. Chen, Z.L. Wang, Irregular wind energy harvesting by a turbine vent triboelectric nanogenerator and its application in a self-powered on-site industrial monitoring system, ACS Appl. Mater. Interfaces 13 (2021) 55136–55144, https://doi.org/10.1021/acsami.1c16680.
[18] B. Chen, Z.L. Wang, Toward a new era of sustainable energy: advanced triboelectric nanogenerator for harvesting high entropy energy, Small 18 (2022), 2107034, https://doi.org/10.1002/smll.202107034.
[19] B.D. Chen, W. Tang, C. He, C.R. Deng, L.J. Yang, L.P. Zhu, J. Chen, J.J. Shao, L. Liu, Z.L. Wang, Water wave energy harvesting and self-powered liquid-surface fluctuation sensing based on bionic-jellyfish triboelectric nanogenerator, Mater. Today 21 (2018) 88–97, https://doi.org/10.1016/j.mattod.2017.10.006.
[20] X. Gao, F. Xing, F. Guo, J. Wen, H. Li, Y. Yang, B. Chen, Z.L. Wang, Strongly enhanced charge density via gradient nano-doping for high performance elastic-material-based triboelectric nanogenerators, Mater. Today 65 (2023) 26–36, https://doi.org/10.1016/j.mattod.2023.03.010.
[21] L. Long, W. Liu, Z. Wang, W. He, G. Li, Q. Tang, H. Guo, X. Pu, Y. Liu, C. Hu, High performance floating self-excited sliding triboelectric nanogenerator for micro mechanical energy harvesting, Nat. Commun. 12 (2021) 4689, https://doi.org/10.1038/s41467-021-25047-y.
[22] Y. Yang, J. Wen, F. Chen, Y. Hao, X. Gao, T. Jiang, B. Chen, Z.L. Wang, Barycenter self-adapting triboelectric nanogenerator for sea water wave high-entropy energy harvesting and self-powered forecasting in marine meteorology, Adv. Funct. Mater. 32 (2022), 2200521, https://doi.org/10.1002/adfm.202200521.
[23] Y. Shang, C. Li, G. Yu, Y. Yang, W. Zhao, W. Tang, High storable power density of triboelectric nanogenerator within centimeter size, Materials 16 (2023) 4669, https://doi.org/10.3390/ma16134669.
[24] L.L. Zu, J. Wen, S.B. Wang, M. Zhang, W.L. Sun, B.D. Chen, Z.L. Wang, Multiangle, self-powered sensor array for monitoring head impacts, Sci. Adv. 9 (2023) 5152, https://doi.org/10.1126/sciadv.adg5152.
[25] E. Su, H. Li, J. Zhang, Z. Xu, B. Chen, L.N.Y. Cao, Z.L. Wang, Rationally designed anti-glare panel arrays as highway wind energy harvester, Adv. Funct. Mater. 33 (2023), 2214934, https://doi.org/10.1002/adfm.202214934.
[26] Z.Y. Huo, D.M. Lee, J.M. Jeong, Y.J. Kim, J. Kim, I.Y. Suh, P. Xiong, S.W. Kim, Microbial disinfection with supercoiling capacitive triboelectric nanogenerator, Adv. Energy Mater. 12 (2022), 2103680, https://doi.org/10.1002/aenm.202103680.
[27] D.M. Lee, N. Rubab, I. Hyun, W. Kang, Y.J. Kim, M. Kang, B.O. Choi, S.W. Kim, Ultrasound-mediated triboelectric nanogenerator for powering on-demand transient electronics, Sci. Adv. 8 (2022) 8, https://doi.org/10.1126/sciadv.abl8423.
[28] M. Seol, S. Kim, Y. Cho, K.E. Byun, H. Kim, J. Kim, S.K. Kim, S.W. Kim, H.J. Shin, S. Park, Triboelectric series of 2D layered materials, Adv. Mater. 30 (2018), 1801210, https://doi.org/10.1002/adma.201801210.
[29] F. Xing, Z. Ou, X. Gao, B. Chen, Z.L. Wang, Harvesting electrical energy from high temperature environment by aerogel nano-covered triboelectric yarns, Adv. Funct. Mater. 32 (2022), 2205275, https://doi.org/10.1002/adfm.202205275.
[30] B. Chen, W. Tang, Z.L. Wang, Advanced 3D printing-based triboelectric nanogenerator for mechanical energy harvesting and self-powered sensing, Mater. Today 50 (2021) 224–238, https://doi.org/10.1016/j.mattod.2021.05.017.
[31] Z. Zhou, X. Li, Y. Wu, H. Zhang, Z. Lin, K. Meng, Z. Lin, Q. He, C. Sun, J. Yang, Z. L. Wang, Wireless self-powered sensor networks driven by triboelectric nanogenerator for in-situ real time survey of environmental monitoring, Nano Energy 53 (2018) 501–507, https://doi.org/10.1016/j.nanoen.2018.08.055.
[32] Y. Liu, W. Yan, J. Han, B. Chen, Z.L. Wang, Aerodynamics-based triboelectric nanogenerator for enhancing multi-operating robustness via mode automatic switching, Adv. Funct. Mater. 32 (2022), 2202964, https://doi.org/10.1002/adfm.202202964.
[33] S. Yong, H. Wang, Z. Lin, X. Li, B. Zhu, L. Yang, W. Ding, R. Liao, J. Wang, Z. L. Wang, Environmental self-adaptive wind energy harvesting technology for self-powered system by triboelectric-electromagnetic hybridized nanogenerator with dual-channel power management topology, Adv. Energy Mater. 12 (2022), 2202469, https://doi.org/10.1002/aenm.202202469.
[34] J. Zhang, P. Chen, L. Zu, J. Yang, Y. Sun, H. Li, B. Chen, Z.L. Wang, Self-powered high-voltage recharging system for removing noxious tobacco smoke by biomimetic hairy-contact triboelectric nanogenerator, Small 18 (2022), 2202835, https://doi.org/10.1002/smll.202202835.
[35] H. Qiu, H. Wang, L. Xu, M. Zheng, Z.L. Wang, Brownian motor inspired monodirectional continuous spinning triboelectric nanogenerators for extracting energy from irregular gentle water waves, Energy Environ. Sci. 16 (2023) 473–483, https://doi.org/10.1039/d2ee03395j.
[36] T. Leclercq, E. de Langre, Vortex-induced vibrations of cylinders bent by the flow, J. Fluids Struct. 80 (2018) 77–93, https://doi.org/10.1016/j.jfluidstructs.2018.03.008.
[37] M.-M. Liu, H.-C. Wang, F.-F. Shao, X. Jin, G.-Q. Tang, F. Yang, Numerical investigation on vortex-induced vibration of an elastically mounted circular cylinder with multiple control rods at low Reynolds number, Appl. Ocean Res. 118 (2022), 102987, https://doi.org/10.1016/j.apor.2021.102987.
[38] B.S. Carmo, S.J. Sherwin, P.W. Bearman, R.H.J. Willden, Flow-induced vibration of a circular cylinder subjected to wake interference at low Reynolds number, J. Fluids Struct. 27 (2011) 503–522, https://doi.org/10.1016/j.jfluidstructs.2011.04.003.
[39] J. Wang, L. Geng, L. Ding, H. Zhu, D. Yurchenko, The state-of-the-art review on energy harvesting from flow-induced vibrations, Appl. Energy 267 (2020), 114902, https://doi.org/10.1016/j.apenergy.2020.114902.
[40] Navrose, S. Mittal, Lock-in in vortex-induced vibration, J. Fluid Mech. 794 (2016) 565–594, https://doi.org/10.1017/jfm.2016.157.
[41] M. Heil, J. Rosso, A.L. Hazel, M. Brøns, Topological fluid mechanics of the formation of the Kármán-vortex street, J. Fluid Mech. 812 (2016) 199–221, https://doi.org/10.1017/jfm.2016.792.

Gao Yu is currently pursuing his master's degree at the College of Physical Science and Engineering Technology of Guangxi University and the Beijing Institute of Nanoenergy and Systems. His research interests are energy harvesting and self-powered sensing.

Wen Jing is a postdoctoral fellow in Beijing Institute of Nanoenergy and Nanosystems, Chinese Academy of Sciences. She received his Ph. D. from School of Materials Science and Engineering in 2020, from Inner Mongolia University of Technology, China. His research interests include triboelectric nanogenerator, self-powered systems, and energy harvesting.

Hao Li is currently a doctoral student at the University of Chinese Academy of Sciences. His research focuses on friction nanogenerators for wind energy harvesting.

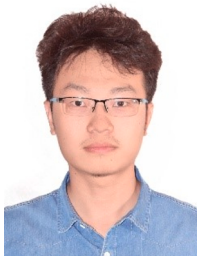

Yurui Shang is currently working toward his M.S. degree in Electrical Engineering with the School of Electrical Engineering, Guangxi University, and the Beijing Institute of Nanoenergy and Nanosystems. His research interests include energy harvesting, the power management circuit of TENG, and Embedded Development.

Zhong Lin Wang is the Hightower Chair in Materials Science and Engineering and Regents' Professor at Georgia Tech., and the chief scientist and director of the Beijing Institute of Nanoenergy and Nanosystems, Chinese Academy of Sciences. His discovery and breakthroughs in developing nanogenerators and self-powered nanosystems establish the principle and technological road map for harvesting mechanical energy from environmental and biological systems for powering personal electronics and future sensor networks. He coined and pioneered the field of piezotronics and piezophototronics.

Baodong Chen is a professor in Beijing Institute of Nanoenergy and Nanosystems, Chinese Academy of Sciences. Prior to joining the faculty at BINN (CAS) in 2018, he was a postdoctoral fellow at National Center for Nanoscience and Technology. His research interests include piezoelectric materials and device, triboelectric nanogenerator, self-powered systems, and 2D and 3D printed flexible electronics.